



MambaAD: Exploring State Space Models for Multi-class Unsupervised Anomaly Detection

Haoyang He^{1*} Yuhu Bai^{1*} Jiangning Zhang² Qingdong He² Hongxu Chen¹

Zhenye Gan² Chengjie Wang² Xiangtai Li³ Guanzhong Tian¹ Lei Xie¹

¹Zhejiang University ²Youtu Lab, Tencent ³Nanyang Technological University

Abstract

Recent advancements in anomaly detection have seen the efficacy of CNN- and transformer-based approaches. However, CNNs struggle with long-range dependencies, while transformers are burdened by quadratic computational complexity. Mamba-based models, with their superior long-range modeling and linear efficiency, have garnered substantial attention. This study pioneers the application of Mamba to multi-class unsupervised anomaly detection, presenting MambaAD, which consists of a pre-trained encoder and a Mamba decoder featuring (Locality-Enhanced State Space) LSS modules at multi-scales. The proposed LSS module, integrating parallel cascaded (Hybrid State Space) HSS blocks and multi-kernel convolutions operations, effectively captures both long-range and local information. The HSS block, utilizing (Hybrid Scanning) HS encoders, encodes feature maps into five scanning methods and eight directions, thereby strengthening global connections through the (State Space Model) SSM. The use of Hilbert scanning and eight directions significantly improves feature sequence modeling. Comprehensive experiments on six diverse anomaly detection datasets and seven metrics demonstrate state-of-the-art performance, substantiating the method's effectiveness. The code and models are available at <https://lewandofskee.github.io/projects/MambaAD>.

1 Introduction

The advent of smart manufacturing has markedly increased the importance of industrial visual Anomaly Detection (AD) in production processes. This technology promises to enhance efficiency, diminish the costs of manual inspections, and elevate product quality along with the stability of production lines. Presently, most methods predominantly utilize a single-class setting [8, 25, 49], where a separate model is trained and tested for each class, leading to considerable increases in training and memory usage. Despite recent progress in introducing multi-class AD techniques [43, 14], there is still significant potential for advancement in terms of both accuracy and efficiency trade-off.

The current unsupervised anomaly detection algorithms can be broadly categorized into three approaches [46, 5]: *Embedding-based* [32, 7, 3, 8], *Synthesizing-based* [44, 20, 49, 25], and *Reconstruction-based* [22, 14]. Despite the promising results of both Synthesizing and Embedding-based methods in AD, these approaches often require extensive design and inflexible frameworks. Reconstruction-based methods, such as RD4AD [8] and UniAD [43], exhibit superior performance and better scalability. RD4AD, as depicted in Fig. 1 (a), employs a pre-trained teacher-student model, comparing anomalies across multi-scale feature levels. While CNN-based RD4AD captures local context effectively, *it lacks the ability to establish long-range dependencies*. UniAD, the first multi-class AD algorithm, relies on a pre-trained encoder and transformer decoder architecture as illustrated in Fig. 1 (b). Despite their superior global modeling capabilities, *transformers are hampered by*

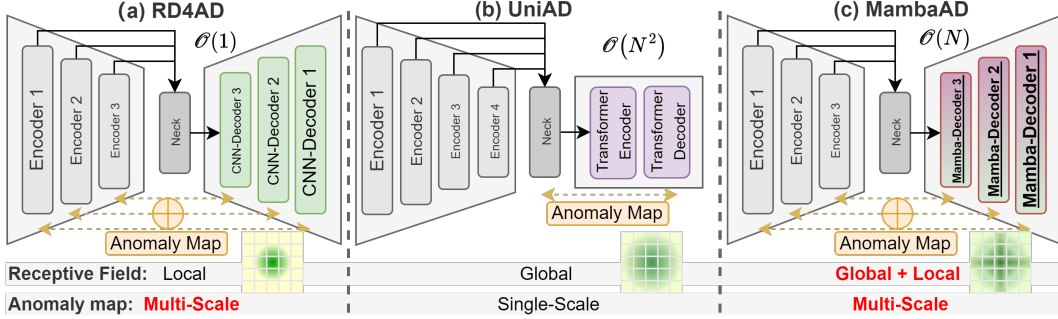


Figure 1: Compared with (a) local CNN-based RD4AD [8] and (b) global Transformer-based UniAD [43], ours MambaAD with linear complexity is capable of integrating the advantages of both global and local modeling, and multi-scale features endow it with more refined prediction accuracy.

quadratic computational complexity, which confines UniAD to anomaly detection on the smallest feature maps, potentially impacting its performance.

Recently, Mamba [11] has demonstrated exceptional performance in large language models, offering significantly lower linear complexity compared to transformers while maintaining comparable effectiveness. Numerous recent studies have incorporated Mamba into the visual domain, sparking a surge of research [24, 51, 36, 18, 33, 39]. This paper pioneers the application of Mamba into the anomaly detection area, introducing MambaAD, as illustrated in Fig. 1 (c). *MambaAD combines global and local modeling capabilities, leveraging its linear complexity to compute anomaly maps across multiple scales.* Notably, it boasts a lower parameter count and computational demand, making it well-suited for practical applications.

Specifically, MambaAD employs a pyramid-structured auto-encoder to reconstruct multi-scale features, utilizing a pre-trained encoder and a novel decoder based on the Mamba architecture. This Mamba-based decoder consists of Locality-Enhanced State Space (LSS) modules at varying scales and quantities. Each LSS module comprises two components: a series of Hybrid State Space (HSS) blocks for global information capture and parallel multi-kernel convolution operations for establishing local connections. The resulting output features integrate the global modeling capabilities of the mamba structure with the local correlation strengths of CNNs. The proposed HSS module investigates five distinct scanning methods and eight scanning directions, with the (Hybrid Scanning) HS encoder and decoder encoding and decoding feature maps into sequences of various scanning methods and directions, respectively. The HSS module enhances the global receptive field across multiple directions, and its use of the Hilbert scanning method [15, 19] is particularly suited to the central concentration of industrial product features. By computing and summing anomaly maps across different feature map scales, MambaAD achieves SoTA performance on several representative AD datasets with seven different metrics for both image- and pixel-level while maintaining a low model parameter count and computational complexity. Our contributions are as follows:

- We introduce MambaAD, which innovatively applies the Mamba framework to address multi-class unsupervised anomaly detection tasks. This approach enables multi-scale training and inference with minimal model parameters and computational complexity.
- We design a Locality-Enhanced State Space (LSS) module, comprising cascaded Mamba-based blocks and parallel multi-kernel convolutions, extracts both global feature correlations and local information associations, achieving a unified model of global and local patterns.
- We have explored a Hybrid State Space (HSS) block, encompassing five methods and eight multi-directional scans, to enhance the global modeling capabilities for complex anomaly detection images across various categories and morphologies.
- We demonstrate the superiority and efficiency of MambaAD in multi-class anomaly detection tasks, achieving SoTA results on **six** distinct AD datasets with **seven** metrics while maintaining remarkably low model parameters and computational complexity.

2 Related Work

2.1 Unsupervised Anomaly Detection

Unsupervised Anomaly Detection. Existing AD methods can be mainly categorized into three types: 1) *Embedding-based methods* focus on encoding RGB images into multi-channel features [32, 7, 3, 8, 6, 34]. These methods typically employ networks pre-trained on ImageNet [9]. PatchCore [32] extracts nominal patch features with a memory bank for measuring the Mahalanobis distance. DifferNet [34] maps the latent multi-channel features into a multivariate Gaussian distribution at multiple scales. [3] is based on a student-teacher framework where student networks are trained to regress the output of a teacher network, which is pre-trained on a large dataset (e.g. ImageNet) of natural image patches. However, the datasets used for these pre-trained models have a significant distribution gap compared to industrial images. 2) *Synthesizing-based methods* synthesize anomalies on normal images [44, 20, 35, 16]. The pseudo-anomalies in DREAM [44] are generated utilizing Perlin noise and texture images. DREAM, taking anomaly mask as output, consists of a reconstruction network and a discriminative network. NSA [35] employs Poisson image editing to create realistic synthetic anomalies by blending scaled patches from different images. Despite the decent performance of such methods, the synthesized anomalies still have a certain gap compared to real-world anomalies. 3) *Reconstruction-based methods* [8, 22, 47] typically focus on self-training encoders and decoders to reconstruct images, reducing reliance on pre-trained models. Autoencoder [31], Transformers[29], Generative Adversarial Networks (GANs) [22, 42] and diffusion models [14, 41] can serve as the backbone for reconstruction networks in anomaly detection. While the model’s generalization can occasionally lead to inaccuracies in pinpointing anomalous areas.

Multi-class Anomaly Detection. Most current works are trained individually on separate categories, which leads to increased time and memory consumption as the number of categories grows, and they are uncongenial to situations with large intra-class diversity. Recently, to address these issues, multi-class unsupervised anomaly detection (MUAD) methods have attracted a lot of interest. UniAD [43] firstly crafts a unified reconstruction framework for anomaly detection. HVQ-Trans [27] utilizes a vector quantization framework in order to prevent learning "identical shortcut". DiAD [14] investigates an anomaly detection framework based on diffusion models, introducing a semantic-guided network to ensure the consistency of reconstructed image semantics. ViTAD [46] further explores the effectiveness of vanilla Vision Transformer (ViT) on multi-class anomaly detection.

2.2 State Space Models

State space models (SSMs) [13, 12, 37, 28, 10] have gained considerable attention due to their efficacy in handling long language sequence modeling. Specifically, structure state-space sequence (S4) [12] efficiently models long-range dependencies (LRDs) through parameterization with a diagonal structure, addressing computational bottlenecks encountered in previous works. Building upon S4, numerous models have been proposed, including S5 [37], H3 [10], and notably, Mamba [11]. Mamba introduces a data-dependent selection mechanism into S4, which provides a novel paradigm distinct from CNNs or Transformers, maintaining linear scalability of long sequences processing.

The tremendous potential of Mamba has sparked a series of excellent works [24, 51, 33, 17, 18, 36, 40, 39, 26, 48, 21] in the vision domain. Vmamba [24] proposes a cross-scan module (CSM) to tackle the direction sensitivity issue between non-causal 2D images and ordered 1D sequences. Moreover, Mamba has found extensive use in the domain of medical image segmentation [33, 23, 40, 39], incorporating Mamba blocks to UNet-like architecture to achieve task-specific architecture. In image restoration, Vmambair [36] introduces an omni-selective scan mechanism, which combines the information from planar modeling with channel modeling in all six directions, overcoming the unidirectional modeling limitations of SSMs. VL-Mamba [30] and Cobra [50] explore the potential of SSMs in multimodal large language models. Besides, ZigMa [17] addresses the spatial continuity in the scan strategy, and it incorporates Mamba into the Stochastic Interpolation framework [1].

In this work, we develop MambaAD to exploit Mamba’s long-range modeling capacity and linear computational efficiency for multi-class unsupervised anomaly detection. This approach innovatively combines SSM’s extensive modeling capabilities with CNNs’ detailed local modeling prowess, resulting in seamless integration.

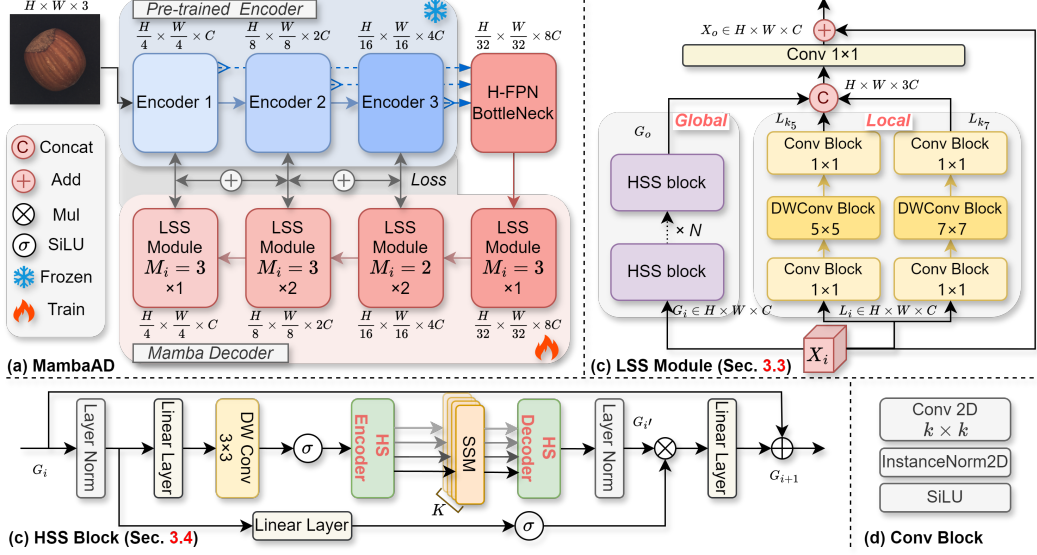


Figure 2: **Overview of the proposed MambaAD**, which employs pyramidal auto-encoder framework to reconstruct multi-scale features by the proposed efficient and effective Locality-Enhanced State Space (LSS) module. Specifically, each LSS consists of: 1) cascaded Hybrid State Space (HSS) blocks to capture global interaction; and 2) parallel multi-kernel convolution operations to replenish local information. Aggregated multi-scale reconstruction error serves as the anomaly map for inference.

3 Method

3.1 Preliminaries

State Space Models [12], inspired by control systems, map a one-dimensional stimulation $x(t) \in \mathbb{R}^L$ to response $y(t) \in \mathbb{R}^L$ through a hidden state $h(t) \in \mathbb{R}^N$, which are formulated as linear ordinary differential equations (ODEs):

$$h'(t) = \mathbf{A}h(t) + \mathbf{B}x(t), \quad y(t) = \mathbf{C}h(t), \quad (1)$$

where the state transition matrix $\mathbf{A} \in \mathbb{R}^{N \times N}$, $\mathbf{B} \in \mathbb{R}^{N \times 1}$ and $\mathbf{C} \in \mathbb{R}^{1 \times N}$ for a state size N .

S4 [12] and Mamba [11] utilize zero-order hold with a timescale parameter Δ to transform the continuous parameters \mathbf{A} and \mathbf{B} from the continuous system into the discrete parameters $\overline{\mathbf{A}}$ and $\overline{\mathbf{B}}$:

$$\overline{\mathbf{A}} = \exp(\Delta \mathbf{A}), \quad \overline{\mathbf{B}} = (\Delta \mathbf{A})^{-1}(\exp(\Delta \mathbf{A}) - \mathbf{I}) \cdot \Delta \mathbf{B}. \quad (2)$$

After the discretization, the discretized model formulation can be represented as:

$$h_t = \overline{\mathbf{A}}h_{t-1} + \overline{\mathbf{B}}x_t, \quad y_t = \mathbf{C}h_t. \quad (3)$$

At last, from the perspective of global convolution, the output can be defined as:

$$\overline{\mathbf{K}} = (\mathbf{C}\overline{\mathbf{B}}, \mathbf{C}\overline{\mathbf{A}}\overline{\mathbf{B}}, \dots, \mathbf{C}\overline{\mathbf{A}}^{L-1}\overline{\mathbf{B}}), \quad \mathbf{y} = \mathbf{x} * \overline{\mathbf{K}}, \quad (4)$$

where $*$ represents convolution operation, L is the length of sequence x , and $\overline{\mathbf{K}} \in \mathbb{R}^L$ is a structured convolutional kernel.

3.2 MambaAD

The MambaAD framework is proposed for multi-class anomaly detection as illustrated in Fig. 2(a). It consists of three main components: a pre-trained CNN-based encoder, a Half-FPN bottleneck, and a Mamba-based decoder. During training, the encoder extracts feature maps at three different scales and inputs them into the H-FPN bottleneck for fusion. The fused output is then fed into

the Mamba Decoder with a depth configuration of [3,4,6,3]. The final loss function is the sum of the mean squared error (MSE) computed across feature maps at three scales. Within the Mamba Decoder, we introduce the Locality-Enhanced State Space (LSS) module. The LSS can be configured with different stages M_i , where each stage represents the number N of Hybrid State Space (HSS) blocks within the module. In this experiment, we employ LSS with $M_i = 3$ and $M_i = 2$ as the primary modules. The LSS module processes the input X_i through HSS blocks that capture global information and through two different scales of depth-wise convolution layers that capture local information. The original input feature dimension is restored through concatenation and convolution operations. The proposed HSS block features a Hybrid Scanning (HS) Encoder and an HS Decoder, which accommodates five distinct scanning methods and eight scanning directions.

3.3 Locality-Enhanced State Space Module

Transformers excel in global modeling and capturing long-range dependencies but tend to overlook local semantic information and exhibit high computational complexity when processing high-resolution features. Conversely, CNNs effectively model local semantics by capturing information from adjacent positions but lack long-range modeling capabilities. To address these limitations, we propose the LSS module in Fig. 2 (b), which incorporates both Mamba-based cascaded HSS blocks for global modeling and parallel multi-kernel depth-wise convolution operations for local information capture.

Specifically, for an input feature $X_i \in \mathbb{R}^{H \times W \times C}$, global features $G_i \in \mathbb{R}^{H \times W \times C}$ enter the HSS blocks while local features $L_i \in \mathbb{R}^{H \times W \times C}$ proceed through a convolutional network. The global features G_i pass through a series of N HSS blocks to obtain global information features G_o .

$$G_o = \text{HSS}_n(\dots(\text{HSS}_2(\text{HSS}_1(G_i)))), \quad (5)$$

where $n \in N$ is the number of HSS blocks. In this study, we primarily use $N = 2$ and $N = 3$, with further ablation experiments presented in Sec. 4.3.

Local features L_i are processed by two parallel depth-wise Conv blocks, each comprising a 1×1 Conv block, an $k \times k$ depth-wise Conv block, and another 1×1 Conv block.

$$L_m = \text{ConvB}_{1 \times 1}(\text{DWConvB}_{k \times k}(\text{ConvB}_{1 \times 1}(L_i))), \quad (6)$$

where k is the kernel size for the depth-wise convolution. $k = 5$ and $k = 7$ are used in this experiment with further ablations in Sec. 4.3. Each convolutional module includes a Conv 2D layer, an Instance Norm 2D normalization layer, and a SiLU activation function as illustrated in Fig. 2 (d). Local and global features are aggregated by concatenation along the channel dimension. The final output X_o of this block is obtained by a 1×1 2D convolution to restore the channel count to match that of the input and a residual connection.

$$X_o = \text{Conv2D}_{1 \times 1}(\text{Concat}(G_o, L_{k_5}, L_{k_7})) + X_i. \quad (7)$$

3.4 Hybrid State Space Block

Following the method outlined in [24, 33], the HSS block is designed for hybrid-method and hybrid-directional scanning and fusion, as depicted in Fig. 2 (c). The HSS block primarily comprises Layer Normalization (LN), Linear Layer, depth-wise convolution, SiLU activation, Hybrid Scanning (HS) encoder \mathcal{E}_{HS} , State Space Models (SSMs), HS decoder \mathcal{D}_{HS} , and residual connections.

$$\begin{aligned} G'_i &= \text{LN}(\mathcal{D}_{HS}(\text{SSMs}(\mathcal{E}_{HS}(\sigma(\text{DWConv}_{3 \times 3}(\text{Linear}(\text{LN}(G_i)))))))), \\ G_{i+1} &= \text{Linear}(G'_i \cdot \sigma(\text{Linear}(\text{LN}(G_i)))) + G_i \end{aligned} \quad (8)$$

Hybrid Scanning methods. Inspired by space-filling curves [45], as shown in Fig. 3, this study explores five different scanning methods: (I) Sweep, (II) Scan, (III) Z-order, (IV) Zigzag, and (V) Hilbert, to assess their impact on the SSM's modeling capabilities. The Hilbert scanning method is ultimately selected for its superior encoding and modeling of local and global information within feature sequences, particularly in mitigating the challenges of modeling long-range dependencies. Further experimental results will be presented in the ablation study. Assuming A is a matrix, A^T is the transpose of A , A^{lr} is the left-right reversal of A , A^{ud} is the up-down reversal of A . The Hilbert

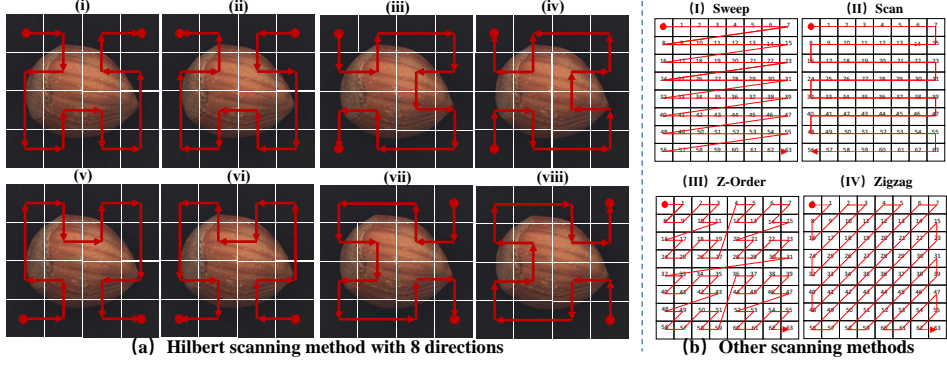


Figure 3: Hybrid Scanning directions and methods. (a) The Hilbert scanning method with 8 scanning directions is used for HS Encoder and Decoder. (b) The other four scanning methods for comparison.

curve can be obtained by an n -order Hilbert matrix:

$$H_{n+1} = \begin{cases} \begin{pmatrix} H_n & 4^n E_n + H_n^T \\ (4^{n+1} + 1)E_n - H_n^{ud} & (3 \times 4^n + 1)E_n - (H_n^{lr})^T \end{pmatrix} & \text{, if } n \text{ is even,} \\ \begin{pmatrix} H_n & (4^{n+1} + 1)E_n - H_n^{lr} \\ 4^n E_n + H_n^T & (3 \times 4^n + 1)E_n - (H_n^T)^{lr} \end{pmatrix} & \text{, if } n \text{ is odd,} \end{cases} \quad (9)$$

where $H_1 = \begin{pmatrix} 1 & 2 \\ 4 & 3 \end{pmatrix}$ and E_n is all-one matrix for n -order.

Hybrid Scanning directions. Following the setup of previous scanning directions, this study supports eight Hilbert-based scanning directions: (i) forward, (ii) reverse, (iii) width-height (wh) forward, (iv) wh reverse, (v) rotated 90 degrees forward, (vi) rotated 90 degrees reverse, (vii) wh rotated 90 degrees forward, and (viii) wh rotated 90 degrees reverse, as illustrated in Fig. 3 (a). Multiple scanning directions enhance the encoding and modeling capabilities of feature sequences, enabling the handling of various types of anomalous features with further ablations in Sec. 4.3.

The HS encoder aims to combine and encode input features according to different scanning methods and directions before feeding them into the SSM to enhance the global modeling capacity of the feature vectors. The HS decoder then decodes the feature vectors output by the SSM back to the original input feature orientation, with the final output obtained by summation.

4 Experiments

4.1 Setups: Datasets, Metrics, and Details

MVTec-AD [2] encompasses a diverse collection of 5 types of textures and 10 types of objects, 5,354 high-resolution images in total. 3,629 normal images are designated for training. The remaining 1,725 images are reserved for testing and include both normal and abnormal samples.

VisA [52] features 12 different objects, incorporating three diverse types: complex structures, multiple instances, and single instances. It consists of a total of 10,821 images, of which 9,621 are normal samples, and 1,200 are anomaly samples.

Real-IAD [38] includes objects from 30 distinct categories, with a collection of 150K high-resolution images, making it larger than previous anomaly detection datasets. It consists of 99,721 normal images and 51,329 anomaly images.

More results on MVTec-3D [4], as well as newly proposed Uni-Medical [46] and COCO-AD [47] datasets, can be viewed in Appendix.

Metrics. For anomaly detection and segmentation, we report Area Under the Receiver Operating Characteristic Curve (AU-ROC), Average Precision [44] (AP) and F1-score-max [52] (F1_max). Additionally, for anomaly segmentation, we also report Area Under the Per-Region-Overlap [3]

Table 1: Quantitative Results on different AD datasets for multi-class setting.

Dataset	Method	Image-level			Pixel-level			mAD
		AU-ROC	AP	F1_max	AU-ROC	AP	F1_max	
MVTec-AD [2]	RD4AD [8]	94.6	96.5	95.2	96.1	48.6	53.8	91.1
	UniAD [43]	96.5	98.8	96.2	96.8	43.4	49.5	90.7
	SimpleNet [25]	95.3	98.4	95.8	96.9	45.9	49.7	86.5
	DeSTSeg [49]	89.2	95.5	91.6	93.1	54.3	50.9	77.1
	DiAD [14]	97.2	99.0	96.5	96.8	52.6	55.5	90.7
	MambaAD (Ours)	98.6	99.6	97.8	97.7	56.3	59.2	93.1
VisA [52]	RD4AD [8]	92.4	92.4	89.6	98.1	38.0	42.6	91.8
	UniAD [43]	88.8	90.8	85.8	98.3	33.7	39.0	85.5
	SimpleNet [25]	87.2	87.0	81.8	96.8	34.7	37.8	81.4
	DeSTSeg [49]	88.9	89.0	85.2	96.1	39.6	43.4	67.4
	DiAD [14]	86.8	88.3	85.1	96.0	26.1	33.0	75.2
	MambaAD (Ours)	94.3	94.5	89.4	98.5	39.4	44.0	91.0
Uni-Medical [46]	RD4AD [8]	75.6	75.8	78.0	96.5	38.7	40.1	86.4
	UniAD [43]	78.5	75.2	76.6	96.4	37.6	40.2	85.0
	SimpleNet [25]	75.6	76.9	76.8	95.9	38.3	39.6	80.5
	DeSTSeg [49]	80.7	79.8	78.7	86.6	38.0	37.5	25.1
	DiAD [14]	80.4	80.1	77.8	95.9	38.0	35.6	85.4
	MambaAD (Ours)	83.7	80.1	82.0	96.9	45.4	47.3	87.5
MVTec-3D [4]	RD4AD [8]	77.9	92.4	91.4	98.4	29.8	36.4	93.5
	UniAD [43]	78.9	93.4	91.4	96.5	21.2	28.0	88.1
	SimpleNet [25]	72.5	91.0	90.3	93.5	18.3	25.3	77.6
	DeSTSeg [49]	79.6	94.1	90.6	95.1	38.1	39.9	46.4
	DiAD [14]	84.6	94.8	95.6	96.4	25.3	32.3	87.8
	MambaAD (Ours)	86.2	95.8	92.8	98.6	37.5	41.1	93.6

(AU-PRO). We further calculate the mean value of the above seven evaluation metrics (denoted as *mAD*) to represent a model’s comprehensive capability [46].

Implementation Details. All input images are resized to a uniform size of 256×256 without additional augmentation for consistency. A pre-trained ResNet34 acts as the feature extractor, while a Mamba decoder of equivalent depth [3,4,6,3] to ResNet34 serves as the student model for training. In the Mamba decoder, the number of cascaded HSS blocks in the second LSS module is set to 2, while all other LSS modules employ 3 cascaded HSS blocks. This experiment employs the Hilbert scanning technique, utilizing eight distinct scanning directions. The AdamW optimizer is employed with a learning rate of 0.005 and a decay rate of 1×10^{-4} . The model undergoes a training period of 500 epochs for the multi-class setting, conducted on a single NVIDIA TESLA V100 32GB GPU. During training, the sum of MSE across different scales is employed as the loss function. In the testing phase, the sum of cosine similarities at various scales is utilized as the anomaly maps.

4.2 Comparison with SoTAs on Different AD datasets

We compared our method with current SoTA methods on a range of datasets utilizing both image-level and pixel-level metrics (*c.f.*, Sec. 4.1). This paper primarily compares with UniAD [43] and DiAD [14] dedicated to MUAD. In addition, we also compare our MambaAD with Reconstruction-based RD4AD [8] and Embedding-based DeSTseg [49]/SimpleNet [25].

Quantitative Results. As shown in Tab. 1, on MVTec-AD dateset, our MambaAD outperforms all the comparative methods and reaches a new SoTA to **98.6/99.6/97.6** and **97.7/56.3/59.2/93.1** in multi-class anomaly detection and segmentation. Specifically, compared to DiAD [14], our proposed MambaAD shows an improvement of **1.4 \uparrow 0.6 \uparrow 1.3 \uparrow** at image-level and **0.9 \uparrow 3.7 \uparrow 3.7 \uparrow 2.4 \uparrow** at pixel-level. Notably, for overall metric mAD of a model, our MambaAD improves by **2.0 \uparrow** , compared with SoTA DiAD. The VisA dataset is more complex and challenging, yet our method still demonstrates excellent performance. As shown in Tab. 1, our MambaAD exceeds the performance of DiAD [14] by **7.5 \uparrow 6.2 \uparrow 4.3 \uparrow** at image-level and by **2.5 \uparrow 13.3 \uparrow 11.0 \uparrow 15.8 \uparrow** . Meanwhile, we achieve an enhancement of **8.7 \uparrow** compared to advanced DiAD on the mAD metric. In addition, the SoTA results on MVTec-3D, Medical and COCO-AD datasets, shown in Tab. 1, illustrates scalability, versatility, and efficacy of our method MambaAD. More details results are presented in Appendix.

Qualitative Results. We conducted qualitative experiments on MVTev-AD and VisA datasets that substantiated the accuracy of our method in anomaly segmentation. Fig. 4 demonstrates that our

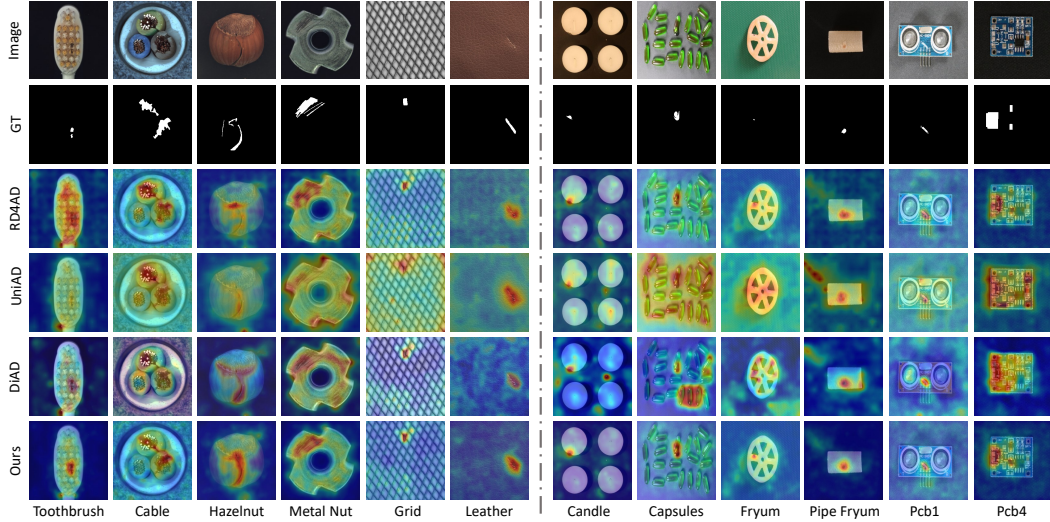


Figure 4: Qualitative visualization for pixel-level anomaly segmentation on MVtec and VisA datasets.

method possesses more precise anomaly segmentation capabilities. Compared to Di4AD, our method delivers more accurate anomaly segmentation, without significant anomaly segmentation bias.

4.3 Ablation and Analysis

Table 2: Ablation studies on the pre-trained backbone and Mamba decoder depth.

Backbone	Decoder Depth	Image-level			Pixel-level				Params(M)	FLOPs(G)
		AU-ROC	AP	F1_max	AU-ROC	AP	F1_max	AU-PRO		
ResNet18	[2,2,2,2]	96.7	98.6	95.8	95.7	47.9	52.4	89.1	14.6	4.3
	[3,4,6,3]	96.6	98.8	96.4	96.8	53.2	56.2	91.8	20.3	6.2
ResNet34	[2,2,2,2]	98.0	99.3	97.0	97.6	55.4	58.2	92.7	20.0	6.5
	[2,9,2,2]	97.6	99.3	97.3	97.7	56.4	59.0	93.2	26.1	7.9
	[3,4,6,3]	98.6	99.6	97.8	97.7	56.3	59.2	93.1	25.7	8.3
ResNet50	[3,4,6,3]	<u>98.4</u>	99.4	97.7	<u>97.7</u>	54.2	57.0	92.3	251.0	60.3
WideResNet50	[3,4,6,3]	98.6	<u>99.5</u>	98.0	98.0	57.9	60.3	93.8	268.0	68.1

Effectiveness comparison of different pre-trained backbone and Mamba decoder depth. First, we compared various pre-trained feature extraction networks, focusing on the popular ResNet series as shown in Tab. 2. When maintaining a consistent Mamba decoder depth, we observed that ResNet18 performed the poorest, despite its minimal model size and computational complexity. ResNet50, with approximately 10 times more parameters and only an 8x increase in computations, did not yield better results. Although WideResNet surpassed ResNet34 in certain metrics, it required nearly 10 times the parameters and computational cost. Consequently, after considering all factors, we elected to use ResNet34 as the backbone feature extractor. Then, we examined the impact of different Mamba decoder depths while keeping the backbone network constant. The depths [2,2,2,2] and [3,4,6,3] corresponded to ResNet18 and ResNet34 depths, respectively, while [2,9,2,2] was the prevalent choice in other methods. Our experiments revealed that the [3,4,6,3] depth, despite a slight increase in parameters and computations, consistently outperformed the other configurations. Therefore, we opted for the [3,4,6,3] configuration as the Mamba decoder’s depth.

Effectiveness and efficiency comparison of different scanning methods and directions. In the initial stage, we compared five distinct scanning methods with an 8-direction scan as shown in Tab. 3. The results indicated that the other four methods produced similar outcomes, albeit marginally inferior to the Hilbert scanning technique at the image level. The Hilbert scanning method demonstrated its practicality for industrial products, potentially reducing false positives. Subsequently, we examined the impact of varying scan directions. As the number of scan directions increased, image-level metrics improved gradually, while pixel-level metrics remained consistent. This suggests that augmenting the

Table 3: Ablations on different scanning methods and directions.

Methods	Directions	Image-level			Pixel-level			
		AU-ROC	AP	F1_max	AU-ROC	AP	F1_max	AU-PRO
Sweep	8	98.1	99.4	97.2	97.5	56.8	58.8	92.9
Scan	8	98.0	99.4	97.2	97.6	56.6	59.0	93.4
Zorder	8	98.1	99.4	97.4	97.6	56.6	59.0	93.0
Zigzag	8	98.2	99.4	97.6	97.6	56.3	58.8	93.1
	2	97.9	99.3	97.1	97.7	56.5	59.2	93.1
Hilbert	4	98.0	99.4	97.0	97.7	56.9	59.1	93.2
	8	98.6	99.6	97.8	97.7	56.3	59.2	93.1

Table 4: Ablation studies on LSS module’s designs.

LSS Design	Local Conv	Kernel Size	Image-level			Pixel-level			
			AU-ROC	AP	F1_max	AU-ROC	AP	F1_max	AU-PRO
$M_i = 1$	Only DWConv	k=1,3	94.6	98.0	96.2	96.7	49.5	52.4	91.3
		k=3,5	94.6	98.0	96.4	96.6	50.1	53.5	91.3
		k=3,7	96.5	98.9	96.7	96.6	51.0	53.8	91.4
		k=1,3,5	94.8	98.2	96.1	95.9	47.7	51.6	89.8
		k=3,5,7	96.5	98.8	96.5	97.2	51.6	55.2	92.2
	DWConv + 1 × 1 Conv	k=1,3,5,7	95.2	98.3	96.5	96.5	49.1	52.6	90.8
		k=3,5	96.1	98.7	96.7	97.2	52.2	55.6	92.5
		k=5,7	95.8	98.6	96.3	97.3	51.7	54.5	92.0
		k=3,5,7	96.0	98.6	96.7	97.3	52.4	55.4	92.2
	Only DWConv	k=3,5	97.3	99.1	97.0	96.9	53.4	55.9	91.5
		k=5,7	95.0	98.2	96.0	96.8	48.6	52.8	91.5
		k=3,5,7	94.6	98.2	95.9	97.1	52.3	55.4	92.3
$M_i = 1, \text{ noskip}$	Only DWConv	k=3,5	95.4	98.4	96.6	97.0	51.6	54.4	91.7
		k=5,7	95.0	98.3	96.3	97.1	50.1	53.9	91.8
		k=3,5,7	96.0	98.7	96.3	97.2	52.3	55.4	92.2
	DWConv + 1 × 1 Conv	k=3,5	98.2	99.2	97.0	97.4	55.7	58.2	92.8
		k=5,7	98.2	99.4	97.4	97.7	56.1	59.0	92.9
		k=3,5,7	98.2	99.3	97.3	97.5	53.9	57.5	92.9
$M_i = 2, M_i = 3$	Only DWConv	k=3,5	98.6	99.5	97.6	97.5	55.3	58.3	92.7
		k=5,7	98.6	99.6	97.8	97.7	56.3	59.2	93.1
	DWConv + 1 × 1 Conv	k=3,5,7	98.1	99.3	97.4	97.5	55.1	57.6	92.8

number of scan directions enhances the global modeling capability of SSM, thereby decreasing the likelihood of image-level misclassification.

Efficiency comparison of different SoTA methods.

In Tab. 5, we compared our model with five SoTA methods in terms of model size and computational complexity. MambaAD exhibits a minimal increase in parameters compared to UniAD. However, MambaAD outperforms it by $4.3 \uparrow$ on the comprehensive metric mAD. Moreover, MambaAD significantly outperforms these other approaches, demonstrating its effectiveness in model lightweight design while maintaining high performance. Particularly, our method MambaAD has achieved a $2.0 \uparrow$ improvement with only $1/50$ the parameters and flops of DiAD.

Effectiveness comparison of different LSS designs. The design of the LSS module, as outlined in Tab. 4, focuses on three distinct design directions: the number of M_i in the LSS module, the configuration of parallel multi-kernel convolution modules, and the kernel size selection for depth-wise convolutions. Initially, we compare scenarios where $M_i = 1$, meaning each LSS module contains a single HSS block, and we experiment with different kernel sizes for depth-wise convolutions alone and configurations flanked by 1×1 convolutions. Subsequently, we contrast the results of configurations without residual connections against those with identical settings but with $M_i = 1$. Finally, we examine the outcomes when $M_i = 2$ and $M_i = 3$ under otherwise consistent settings. Analysis reveals that with $M_i = 1$, regardless of the presence of residual connections, the results are inferior to those with $M_i = 2$ and $M_i = 3$. Moreover, using only depth-wise convolution blocks with $M_i = 1$, a comparison of parallel depth-wise convolutions with varying kernel sizes indicates that smaller kernels, such as $k = 1$, significantly degrade performance. Therefore, subsequent comparative experiments focus on larger convolution kernels. In the absence of residual connections, some metrics may surpass those with residual connections, but the longer training time and difficulty in convergence

Table 5: Efficiency comparison of SoTA methods.

Method	Params(M)	FLOPs(G)	mAD
RD4AD[8]	80.6	28.4	82.3
UniAD [43]	24.5	3.6	81.7
DeSTSeg [49]	35.2	122.7	81.2
SimpleNet [25]	72.8	16.1	77.1
DiAD [14]	1331.3	451.5	84.0
MambaAD (Ours)	25.7	8.3	86.0

preclude their use in further experiments. In configurations with $M_i = 2$ and $M_i = 3$, we find that depth-wise convolution blocks augmented with 1×1 convolutions exhibit superior performance. Additionally, kernels sized $k = 5$ and $k = 7$ are more suitable for extracting local features and establishing local information associations. Consequently, in this study, we opt for a quantity of HSS blocks with $M_i = 2$ and $M_i = 3$, and we employ parallel depth-wise convolution blocks with kernels sized $k = 5$ and $k = 7$, complemented by 1×1 convolutions before and after.

5 Conclusion

This paper introduces MambaAD, the first application of the Mamba framework to AD. MambaAD consists of a pre-trained encoder and a Mamba decoder, with a novel LSS module employed at different scales and depths. The LSS module, composed of sequential HSS modules and parallel multi-core convolutional networks, combines Mamba’s global modeling prowess with CNN-based local feature correlation. The HSS module employs HS encoders to encode input features into five scanning patterns and eight directions, which facilitate the modeling of feature sequences in industrial products at their central positions. Extensive experiments on six diverse AD datasets and seven evaluation metrics demonstrate the effectiveness of our approach in achieving SoTA performance.

Broader Impact. This study marks our initial attempt to apply Mamba in anomaly detection, laying a foundation for future research. We hope the proposed MambaAD can inspire lightweight and efficient designs in AD.

References

- [1] M. S. Albergo, N. M. Boffi, and E. Vanden-Eijnden. Stochastic interpolants: A unifying framework for flows and diffusions. *arXiv preprint arXiv:2303.08797*, 2023. 3
- [2] P. Bergmann, M. Fauser, D. Sattlegger, and C. Steger. Mvtec ad—a comprehensive real-world dataset for unsupervised anomaly detection. In *CVPR*, 2019. 6, 7
- [3] P. Bergmann, M. Fauser, D. Sattlegger, and C. Steger. Uninformed students: Student-teacher anomaly detection with discriminative latent embeddings. In *CVPR*, 2020. 1, 3, 6
- [4] P. Bergmann, X. Jin, D. Sattlegger, and C. Steger. The mvtec 3d-ad dataset for unsupervised 3d anomaly detection and localization. In *VISAPP*, 2022. 6, 7
- [5] Y. Cao, X. Xu, J. Zhang, Y. Cheng, X. Huang, G. Pang, and W. Shen. A survey on visual anomaly detection: Challenge, approach, and prospect. *arXiv preprint arXiv:2401.16402*, 2024. 1
- [6] N. Cohen and Y. Hoshen. Sub-image anomaly detection with deep pyramid correspondences. *arXiv preprint arXiv:2005.02357*, 2020. 3
- [7] T. Defard, A. Setkov, A. Loesch, and R. Audigier. Padim: a patch distribution modeling framework for anomaly detection and localization. In *ICPR*, 2021. 1, 3
- [8] H. Deng and X. Li. Anomaly detection via reverse distillation from one-class embedding. In *CVPR*, 2022. 1, 2, 3, 7, 9, 13, 14, 15
- [9] J. Deng, W. Dong, R. Socher, L.-J. Li, K. Li, and L. Fei-Fei. Imagenet: A large-scale hierarchical image database. In *CVPR*, 2009. 3
- [10] D. Y. Fu, T. Dao, K. K. Saab, A. W. Thomas, A. Rudra, and C. Ré. Hungry hungry hippos: Towards language modeling with state space models. In *ICLR*, 2022. 3
- [11] A. Gu and T. Dao. Mamba: Linear-time sequence modeling with selective state spaces. *arXiv preprint arXiv:2312.00752*, 2023. 2, 3, 4
- [12] A. Gu, K. Goel, and C. Ré. Efficiently modeling long sequences with structured state spaces. In *ICLR*, 2021. 3, 4
- [13] A. Gu, I. Johnson, K. Goel, K. Saab, T. Dao, A. Rudra, and C. Ré. Combining recurrent, convolutional, and continuous-time models with linear state space layers. In *NeurIPS*, 2021. 3

[14] H. He, J. Zhang, H. Chen, X. Chen, Z. Li, X. Chen, Y. Wang, C. Wang, and L. Xie. A diffusion-based framework for multi-class anomaly detection. In *AAAI*, 2024. 1, 3, 7, 9, 13, 14, 15

[15] D. Hilbert and D. Hilbert. Über die stetige abbildung einer linie auf ein flächenstück. *Dritter Band: Analysis· Grundlagen der Mathematik· Physik Verschiedenes: Nebst Einer Lebensgeschichte*, 1935. 2

[16] T. Hu, J. Zhang, R. Yi, Y. Du, X. Chen, L. Liu, Y. Wang, and C. Wang. Anomalydiffusion: Few-shot anomaly image generation with diffusion model. In *AAAI*, 2024. 3

[17] V. T. Hu, S. A. Baumann, M. Gui, O. Grebenkova, P. Ma, J. Fischer, and B. Ommer. Zigma: Zigzag mamba diffusion model. *arXiv preprint arXiv:2403.13802*, 2024. 3

[18] T. Huang, X. Pei, S. You, F. Wang, C. Qian, and C. Xu. Localmamba: Visual state space model with windowed selective scan. *arXiv preprint arXiv:2403.09338*, 2024. 2, 3

[19] N. Jiang, L. Wang, and W.-Y. Wu. Quantum hilbert image scrambling. *International Journal of Theoretical Physics*, 2014. 2

[20] C.-L. Li, K. Sohn, J. Yoon, and T. Pfister. Cutpaste: Self-supervised learning for anomaly detection and localization. In *CVPR*, 2021. 1, 3

[21] X. Li, H. Yuan, W. Li, H. Ding, S. Wu, W. Zhang, Y. Li, K. Chen, and C. C. Loy. Omg-seg: Is one model good enough for all segmentation? In *CVPR*, 2024. 3

[22] Y. Liang, J. Zhang, S. Zhao, R. Wu, Y. Liu, and S. Pan. Omni-frequency channel-selection representations for unsupervised anomaly detection. *TIP*, 2023. 1, 3

[23] J. Liu, H. Yang, H.-Y. Zhou, Y. Xi, L. Yu, Y. Yu, Y. Liang, G. Shi, S. Zhang, H. Zheng, et al. Swin-umamba: Mamba-based unet with imagenet-based pretraining. *arXiv preprint arXiv:2402.03302*, 2024. 3

[24] Y. Liu, Y. Tian, Y. Zhao, H. Yu, L. Xie, Y. Wang, Q. Ye, and Y. Liu. Vmamba: Visual state space model. *arXiv preprint arXiv:2401.10166*, 2024. 2, 3, 5

[25] Z. Liu, Y. Zhou, Y. Xu, and Z. Wang. Simplenet: A simple network for image anomaly detection and localization. In *CVPR*, 2023. 1, 7, 9, 13, 14, 15

[26] S. Long, Q. Zhou, X. Li, X. Lu, C. Ying, L. Ma, Y. Luo, and S. Yan. Dgmamba: Domain generalization via generalized state space model. *arXiv*, 2024. 3

[27] R. Lu, Y. Wu, L. Tian, D. Wang, B. Chen, X. Liu, and R. Hu. Hierarchical vector quantized transformer for multi-class unsupervised anomaly detection. In *NeurIPS*, 2023. 3

[28] H. Mehta, A. Gupta, A. Cutkosky, and B. Neyshabur. Long range language modeling via gated state spaces. In *ICLR*, 2022. 3

[29] J. Pirnay and K. Chai. Inpainting transformer for anomaly detection. In *ICIP*, 2022. 3

[30] Y. Qiao, Z. Yu, L. Guo, S. Chen, Z. Zhao, M. Sun, Q. Wu, and J. Liu. Vl-mamba: Exploring state space models for multimodal learning. *arXiv preprint arXiv:2403.13600*, 2024. 3

[31] N.-C. Ristea, N. Madan, R. T. Ionescu, K. Nasrollahi, F. S. Khan, T. B. Moeslund, and M. Shah. Self-supervised predictive convolutional attentive block for anomaly detection. In *CVPR*, 2022. 3

[32] K. Roth, L. Pemula, J. Zepeda, B. Schölkopf, T. Brox, and P. Gehler. Towards total recall in industrial anomaly detection. In *CVPR*, 2022. 1, 3

[33] J. Ruan and S. Xiang. Vm-unet: Vision mamba unet for medical image segmentation. *arXiv preprint arXiv:2402.02491*, 2024. 2, 3, 5

[34] M. Rudolph, B. Wandt, and B. Rosenhahn. Same same but differnet: Semi-supervised defect detection with normalizing flows. In *WACV*, 2021. 3

[35] H. M. Schlüter, J. Tan, B. Hou, and B. Kainz. Natural synthetic anomalies for self-supervised anomaly detection and localization. In *ECCV*, 2022. 3

[36] Y. Shi, B. Xia, X. Jin, X. Wang, T. Zhao, X. Xia, X. Xiao, and W. Yang. Vmambair: Visual state space model for image restoration. *arXiv preprint arXiv:2403.11423*, 2024. 2, 3

[37] J. T. Smith, A. Warrington, and S. W. Linderman. Simplified state space layers for sequence modeling. In *ICLR*, 2022. 3

[38] C. Wang, W. Zhu, B.-B. Gao, Z. Gan, J. Zhang, Z. Gu, S. Qian, M. Chen, and L. Ma. Real-iad: A real-world multi-view dataset for benchmarking versatile industrial anomaly detection. In *CVPR*, 2024. 6

[39] Z. Wang, J.-Q. Zheng, Y. Zhang, G. Cui, and L. Li. Mamba-unet: Unet-like pure visual mamba for medical image segmentation. *arXiv preprint arXiv:2402.05079*, 2024. 2, 3

[40] R. Wu, Y. Liu, P. Liang, and Q. Chang. H-vmunet: High-order vision mamba unet for medical image segmentation. *arXiv preprint arXiv:2403.13642*, 2024. 3

[41] J. Wyatt, A. Leach, S. M. Schmon, and C. G. Willcocks. Anoddpdm: Anomaly detection with denoising diffusion probabilistic models using simplex noise. In *CVPR*, 2022. 3

[42] X. Yan, H. Zhang, X. Xu, X. Hu, and P.-A. Heng. Learning semantic context from normal samples for unsupervised anomaly detection. In *AAAI*, 2021. 3

[43] Z. You, L. Cui, Y. Shen, K. Yang, X. Lu, Y. Zheng, and X. Le. A unified model for multi-class anomaly detection. In *NeurIPS*, 2022. 1, 2, 3, 7, 9, 13, 14, 15

[44] V. Zavrtanik, M. Kristan, and D. Skočaj. Draem-a discriminatively trained reconstruction embedding for surface anomaly detection. In *ICCV*, 2021. 1, 3, 6

[45] J. Zhang, C. Xu, J. Li, W. Chen, Y. Wang, Y. Tai, S. Chen, C. Wang, F. Huang, and Y. Liu. Analogous to evolutionary algorithm: Designing a unified sequence model. *NeurIPS*, 2021. 5

[46] J. Zhang, X. Chen, Y. Wang, C. Wang, Y. Liu, X. Li, M.-H. Yang, and D. Tao. Exploring plain vit reconstruction for multi-class unsupervised anomaly detection. *arXiv preprint arXiv:2312.07495*, 2023. 1, 3, 6, 7

[47] J. Zhang, X. Li, G. Tian, Z. Xue, Y. Liu, G. Pang, and D. Tao. Learning feature inversion for multi-class unsupervised anomaly detection under general-purpose coco-ad benchmark. *arXiv*, 2024. 3, 6

[48] T. Zhang, X. Li, H. Yuan, S. Ji, and S. Yan. Point cloud mamba: Point cloud learning via state space model. *arXiv preprint arXiv:2403.00762*, 2024. 3

[49] X. Zhang, S. Li, X. Li, P. Huang, J. Shan, and T. Chen. Destseg: Segmentation guided denoising student-teacher for anomaly detection. In *CVPR*, 2023. 1, 7, 9, 13, 14, 15

[50] H. Zhao, M. Zhang, W. Zhao, P. Ding, S. Huang, and D. Wang. Cobra: Extending mamba to multi-modal large language model for efficient inference. *arXiv preprint arXiv:2403.14520*, 2024. 3

[51] L. Zhu, B. Liao, Q. Zhang, X. Wang, W. Liu, and X. Wang. Vision mamba: Efficient visual representation learning with bidirectional state space model. *arXiv preprint arXiv:2401.09417*, 2024. 2, 3

[52] Y. Zou, J. Jeong, L. Pemula, D. Zhang, and O. Dabeer. Spot-the-difference self-supervised pre-training for anomaly detection and segmentation. In *ECCV*, 2022. 6, 7

Appendix

Overview

The supplementary material presents the following sections to strengthen the main manuscript:

- **Sec. A** shows more quantitative results for each category on the MVTec-AD dataset.
- **Sec. B** shows more quantitative results for each category on the VisA dataset.
- **Sec. C** shows more quantitative results for each category on the MVTec-3D dataset.
- **Sec. D** shows more quantitative results for each category on the Uni-Medical dataset.
- **Sec. E** shows more quantitative results for each category on the COCO-AD dataset.

A More Quantitative Results for Each Category on The MVTec-AD Dataset.

Tab. A1 and Tab. A2 respectively present the results of image-level anomaly detection and pixel-level anomaly localization quantitative outcomes across all categories within the MVTec-AD dataset. The results further demonstrate the superiority of our method over various SoTA approaches.

Table A1: Comparison with SOTA methods on **MVTec-AD** dataset for multi-class anomaly detection with AU-ROC/AP/F1_max metrics.

Method →	RD4AD [8]	UniAD [43]	SimpleNet [25]	DeSTSeg [49]	DiAD [14]	MambaAD
Category ↓	CVPR'22	NeurIPS'22	CVPR'23	CVPR'23	AAAI'24	ours
Objects	Bottle	99.6/99.9/98.4	99.7/100/100.	100/100/100.	98.7/99.6/96.8	99.7/96.5/91.8
	Cable	84.1/89.5/82.5	95.2/95.9/88.0	97.5/98.5/94.7	89.5/94.6/85.9	94.8/98.8/95.2
	Capsule	94.1/96.9/ 96.9	86.9/97.8/94.4	90.7/97.9/93.5	82.8/95.9/92.6	89.0/97.5/95.5
	Hazelnut	60.8/69.8/86.4	99.8/100/99.3	99.9/99.9/99.3	98.8/99.2/98.6	99.5/99.7/97.3
	Metal Nut	100/100/99.	99.2/99.9/ 99.5	96.9/99.3/96.1	92.9/98.4/92.2	99.1/96.0/91.6
	Pill	97.5/99.6/96.8	93.7/98.7/95.7	88.2/97.7/92.5	77.1/94.4/91.7	95.7/98.5/94.5
	Screw	97.7/99.3/95.8	87.5/96.5/89.0	76.7/90.6/87.7	69.9/88.4/85.4	90.7/99.7/97.9
	Toothbrush	97.2/99.0/94.7	94.2/97.4/95.2	89.7/95.7/92.3	71.7/89.3/84.5	99.7/99.9/99.2
	Transistor	94.2/95.2/90.0	99.8/98.0/93.8	99.2/98.7/97.6	78.2/79.5/68.8	98.8/99.6/97.4
Textures	Zipper	99.5/99.9/99.2	95.8/99.5/97.1	99.0/99.7/98.3	88.4/96.3/93.1	95.1/99.1/94.4
	Carpet	98.5/99.6/97.2	99.8/99.9/99.4	95.7/98.7/93.2	95.9/98.8/94.9	99.4/99.9/99.4
	Grid	98.0/99.4/96.5	98.2/99.5/97.3	97.6/99.2/96.4	97.9/99.2/96.6	98.5/99.8/97.7
	Leather	100/100/100.	100/100/100.	100/100/100.	99.2/99.8/98.9	99.8/99.7/97.6
	Tile	98.3/99.3/96.4	99.3/99.8/98.2	99.3/99.8/98.8	97.0/98.9/95.3	96.8/99.9/98.4
	Wood	99.2/99.8/98.3	98.6/99.6/96.6	98.4/99.5/96.7	99.9/100/99.2	99.7/100/100.
Mean		94.6/96.5/95.2	96.5/98.8/96.2	95.3/98.4/95.8	89.2/95.5/91.6	97.2/99.0/96.5
						98.6/99.6/97.8

Table A2: Comparison with SOTA methods on **MVTec-AD** dataset for multi-class anomaly localization with AU-ROC/AP/F1_max/AU-PRO metrics.

Method →	RD4AD [8]	UniAD [43]	SimpleNet [25]	DeSTSeg [49]	DiAD [14]	MambaAD
Category ↓	CVPR'22	NeurIPS'22	CVPR'23	CVPR'23	AAAI'24	(ours)
Objects	Bottle	97.8/68.2/67.6/94.0	98.1/66.0/69.2/93.1	97.2/53.8/62.4/89.0	93.3/61.7/56.0/67.5	98.4/52.2/54.8/86.6
	Cable	85.1/26.3/33.6/75.1	97.3/39.9/45.2/86.1	96.7/42.4/51.2/85.4	89.3/37.5/40.5/49.4	96.8/50.1/57.8/80.5
	Capsule	98.8/43.4/50.0/94.8	98.5/42.7/46.5/92.1	98.5/5.4/44.3/84.5	95.8/47.9/48.9/62.1	97.1/42.0/45.3/87.2
	Hazelnut	97.9/36.2/51.6/92.7	98.1/55.2/56.8/94.1	98.4/44.6/51.4/87.4	98.2/65.8/61.6/84.5	98.3/79.2/80.4/91.5
	Metal Nut	94.8/55.5/56.6/49.1	62.7/14.6/29.2/81.8	98.0/83.1/79.4/85.2	84.2/42.0/22.8/53.0	97.3/30.0/38.3/90.6
	Pill	97.5/63.4/65.2/95.8	95.0/44.0/53.9/95.3	96.5/72.4/67.7/81.9	96.2/61.7/41.8/27.9	95.7/46.0/51.6/89.0
	Screw	99.4/40.2/44.6/96.8	98.3/28.7/37.6/95.2	96.5/15.9/23.2/84.0	93.8/19.9/25.3/47.3	97.9/60.6/59.6/95.0
	Toothbrush	99.0/53.6/58.8/92.0	98.4/34.9/45.7/87.9	98.4/46.9/52.5/87.4	96.2/52.9/58.8/30.9	99.0/78.7/72.8/95.0
	Transistor	85.9/42.3/45.2/74.7	97.9/59.5/64.6/93.5	95.8/58.2/56.0/83.2	73.6/38.4/39.2/43.9	95.1/15.6/31.7/90.0
Textures	Zipper	98.5/53.9/60.3/94.1	96.8/40.1/49.9/92.6	97.9/53.4/54.6/90.7	97.3/64.7/59.2/66.9	96.2/60.7/60.0/91.6
	Carpet	99.0/58.5/60.4/95.1	98.5/49.9/51.1/94.4	97.4/38.7/43.2/90.6	93.6/59.9/58.9/89.3	98.6/42.2/46.4/90.6
	Grid	96.5/23.0/28.4/97.0	63.1/ 0.7/ 1.9/92.9	98.6/20.5/27.6/88.6/	97.0/42.1/46.9/86.8	96.6/66.0/64.1/94.0
	Leather	99.3/33.0/45.1/97.4	98.8/32.9/34.4/96.8	98.7/28.5/32.9/92.7	99.5/71.5/66.5/91.1	98.8/56.1/62.3/91.3
	Tile	95.3/48.5/60.5/85.8	91.8/42.1/50.6/78.4	95.7/60.5/59.9/90.6	93.0/71.0/66.2/87.1	92.4/65.7/64.1/90.7
	Wood	95.3/47.8/51.0/90.0	93.2/37.2/41.5/86.7	91.4/34.8/39.7/76.3	95.9/77.3/71.3/83.4	93.3/43.3/43.5/97.5
Mean		96.1/48.6/53.8/91.1	96.8/43.4/49.5/90.7	96.9/45.9/49.7/86.5	93.1/54.3/50.9/64.8	96.8/52.6/55.5/90.7
						97.7/56.3/59.2/93.1

B More Quantitative Results for Each Category on The VisA Dataset.

Tab. A3 and Tab. A4 respectively present the results of image-level anomaly detection and pixel-level anomaly localization quantitative outcomes across all categories within the VisA dataset. The results further demonstrate the superiority of our method over various SoTA approaches.

Table A3: Comparison with SOTA methods on **VisA** dataset for multi-class anomaly detection with AU-ROC/AP/F1_max metrics.

Method → Category ↓	RD4AD [8] CVPR'22	UniAD [43] NeurIPS'22	SimpleNet [25] CVPR'23	DeSTSeg [49] CVPR'23	DiAD [14] AAAI'24	MambaAD (ours)
pcb1	96.2/95.5/91.9	92.8/92.7/87.8	91.6/91.9/86.0	87.6/83.1/83.7	88.1/88.7/80.7	95.4/93.0/91.6
pcb2	97.8/97.8/94.2	87.8/87.7/83.1	92.4/93.3/84.5	86.5/85.8/82.6	91.4/91.4/84.7	94.2/93.7/89.3
pcb3	96.4/96.2/91.0	78.6/78.6/76.1	89.1/91.1/82.6	93.7/95.1/87.0	86.2/87.6/77.6	93.7/94.1/86.7
pcb4	99.9/99.9/99.0	98.8/98.8/94.3	97.0/97.0/93.5	97.8/97.8/92.7	99.6/99.5/97.0	99.9/99.9/98.5
macaroni1	75.9/ 1.5/76.8	79.9/79.8/72.7	85.9/82.5/73.1	76.6/69.0/71.0	85.7/85.2/78.8	91.6/89.8/81.6
macaroni2	88.3/84.5/83.8	71.6/71.6/69.9	68.3/54.3/59.7	68.9/62.1/67.7	62.5/57.4/69.6	81.6/78.0/73.8
capsules	82.2/90.4/81.3	55.6/55.6/76.9	74.1/82.8/74.6	87.1/93.0/84.2	58.2/69.0/78.5	91.8/95.0/88.8
candle	92.3/92.9/86.0	94.1/94.0/86.1	84.1/73.3/76.6	94.9/94.8/89.2	92.8/92.0/87.6	96.8/96.9/90.1
cashew	92.0/95.8/90.7	92.8/92.8/91.4	88.0/91.3/84.7	92.0/96.1/88.1	91.5/95.7/89.7	94.5/97.3/91.1
chewinggum	94.9/97.5/92.1	96.3/96.2/95.2	96.4/98.2/93.8	95.8/98.3/94.7	99.1/99.5/95.9	97.7/98.9/94.2
fryum	95.3/97.9/91.5	83.0/83.0/85.0	88.4/93.0/83.3	92.1/96.1/89.5	89.8/95.0/87.2	95.2/97.7/90.5
pipe_fryum	97.9/98.9/96.5	94.7/94.7/93.9	90.8/95.5/88.6	94.1/97.1/91.9	96.2/98.1/93.7	98.7/99.3/97.0
Mean	92.4/92.4/89.6	85.5/85.5/84.4	87.2/87.0/81.8	88.9/89.0/85.2	86.8/88.3/85.1	94.3/94.5/89.4

Table A4: Comparison with SOTA methods on **VisA** dataset for multi-class anomaly localization with AU-ROC/AP/F1_max/AU-PRO metrics.

Method → Category ↓	RD4AD [8] CVPR'22	UniAD [43] NeurIPS'22	SimpleNet [25] CVPR'23	DeSTSeg [49] CVPR'23	DiAD [14] AAAI'24	MambaAD (ours)
pcb1	99.4/66.2/62.4/95.8	93.3/ 3.9/ 8.3/64.1	99.2/ 86.1/78.8/83.6	95.8/46.4/49.0/83.2	98.7/49.6/52.8/80.2	99.8/77.1/72.4/92.8
pcb2	98.0/22.3/30.0/90.8	93.9/ 4.2/ 9.2/66.9	96.6/ 8.9/18.6/85.7	97.3/ 14.6/28.2/79.9	95.2/ 7.5/16.7/67.0	98.9/13.3/23.4/89.6
pcb3	97.9/26.2/35.2/93.9	97.3/13.8/21.9/70.6	97.2/31.0/36.1/85.1	97.7/28.1/33.4/62.4	96.7/ 8.0/18.8/68.9	99.1/18.3/27.4/89.1
pcb4	97.8/31.4/37.0/88.7	94.9/14.7/22.9/72.3	93.9/23.9/32.9/61.1	95.8/ 53.0/53.2/76.9	97.0/17.6/27.2/85.0	98.6/47.0/46.9/87.6
macaroni1	99.4/ 2.9/6.9/95.3	97.4/ 3.7/ 9.7/84.0	98.9/ 3.5/ 8.4/92.0	99.1/ 5.8/13.4/62.4	94.1/10.2/16.7/68.5	99.5/17.5/27.6/95.2
macaroni2	99.7/13.2/21.8/97.4	95.2/ 0.9/ 4.3/76.6	93.2/ 0.6/ 3.9/77.8	98.5/ 6.3/14.4/70.0	93.6/ 0.9/ 2.8/73.1	99.5/ 9.2/16.1/96.2
capsules	99.4/60.4/60.8/93.1	88.7/ 3.0/ 7.4/43.7	97.1/52.9/53.3/73.7	96.9/93.3/2/ 9.1/76.7	97.3/10.0/21.0/77.9	99.1/61.3/59.8/91.8
candle	99.1/25.3/35.8/94.9	98.5/17.6/27.9/91.6	97.6/ 8.4/16.5/87.6	98.7/ 39.9/45.8/69.0	97.3/12.8/22.8/89.4	99.0/23.2/32.4/ 95.5
cashew	91.7/44.2/49.7/86.2	98.6/51.7/58.3/ 87.9	98.9/68.9/66.0/84.1	87.9/47.6/52.1/66.3	90.9/53.1/60.9/61.8	94.3/46.8/51.4/87.8
chewinggum	98.7/59.9/61.7/76.9	98.8/54.9/56.1/81.3	97.9/26.8/29.8/78.3	98.8/86.9/81.0/68.3	94.7/11.9/25.8/59.5	98.1/57.5/59.9/ 79.7
fryum	97.0/47.6/51.5/93.4	95.9/34.0/40.6/76.2	93.0/39.1/45.4/85.1	88.1/35.2/38.5/47.7	97.6/58.6/60.1/81.3	96.9/47.8/51.9/91.6
pipe_fryum	99.1/56.8/58.8/ 95.4	98.9/50.2/57.7/91.5	98.5/65.6/63.4/83.0	98.9/ 78.8/72.7/45.9	99.4/72.7/69.9/89.9	99.1/53.5/58.5/ 95.1
Mean	98.1/38.0/42.6/ 91.8	95.9/21.0/27.0/75.6	96.8/34.7/37.8/81.4	96.1/ 39.6/43.4/67.4	96.0/26.1/33.0/75.2	98.5/39.4/44.0/91.0

C More Quantitative Results for Each Category on The MVTec-3D Dataset.

Tab. A5 and Tab. A6 respectively present the results of image-level anomaly detection and pixel-level anomaly localization quantitative outcomes across all categories within the MVTec-3D dataset. The results further demonstrate the superiority of our method over various SoTA approaches.

Table A5: Comparison with SOTA methods on **MVTec-3D** dataset for multi-class anomaly detection with AU-ROC/AP/F1_max metrics.

Method → Category ↓	RD4AD [8] CVPR'22	UniAD [43] NeurIPS'22	SimpleNet [25] CVPR'23	DeSTSeg [49] CVPR'23	DiAD [14] AAAI'24	MambaAD (ours)
bagel	82.5/95.4/89.6	82.7/95.8/89.3	76.2/93.3/89.3	89.7/97.4/92.4	100./100./100.	87.7/96.7/92.2
cable gland	90.1/97.5/92.6	89.8/97.2/ 93.9	70.3/91.0/90.2	84.8/95.7/91.5	68.1/91.0/92.3	94.3/98.6/93.5
carrot	87.3/96.7/93.2	76.8/93.8/92.5	71.4/92.6/91.2	79.1/94.7/91.0	94.4/99.3/98.0	90.7/97.7/95.0
cookie	46.0/77.4/88.0	77.3/93.5/88.0	66.7/87.6/88.4	67.4/89.8/88.0	69.4/78.8/ 90.9	61.2/87.5/88.4
dowel	96.7/79.8/97.6	96.7/99.3/96.2	83.7/95.1/91.7	77.3/94.3/88.9	98.0/99.3/97.3	97.6/ 99.5/96.6
foam	74.3/92.9/90.6	70.5/92.4/88.9	77.4/94.2/89.7	77.9/94.7/88.9	100./100./100.	84.0/95.8/90.4
peach	64.3/84.8/90.6	70.0/91.0/90.5	62.0/86.9/89.7	82.2/95.3/90.7	58.0/91.3/ 94.3	92.8/98.1/94.3
potato	62.5/88.5/90.5	51.6/81.8/89.3	56.7/82.2/89.8	62.9/87.8/90.9	76.3/94.3/95.0	66.8/88.6/90.5
rope	96.3/98.5/93.2	97.4/99.0/95.5	95.6/98.4/94.7	93.5/97.4/92.5	89.2/95.4/91.9	97.4/98.9/94.7
tire	79.2/93.0/88.4	75.7/90.7/89.7	65.3/86.8/87.9	80.8/93.6/91.5	92.7/98.9/95.8	90.0/97.0/91.9
Mean	77.9/92.4/91.4	78.9/93.4/91.4	72.5/91.0/90.3	79.6/94.1/90.6	84.6/94.8/95.6	86.2/95.8/92.8

D More Quantitative Results for Each Category on The Uni-Medical Dataset.

Tab. A7 and Tab. A8 respectively present the results of image-level anomaly detection and pixel-level anomaly localization quantitative outcomes across all categories within the Uni-Medical dataset. The results further demonstrate the superiority of our method over various SoTA approaches.

Table A6: Comparison with SOTA methods on **MVTec-3D** dataset for multi-class anomaly detection with AU-ROC/AP/F1_max/AU-PRO metrics.

Method →	RD4AD [8] CVPR'22	UniAD [43] NeurIPS'22	SimpleNet [25] CVPR'23	DeSTSeg [49] CVPR'23	DiAD [14] AAAI'24	MambaAD (ours)
Category ↓						
bagel	98.6/39.0/45.1/91.3	97.6/30.4/35.8/84.4	93.2/23.6/30.9/70.4	98.7/53.0/52.9/77.6	98.5/49.6/ 54.2/93.8	98.5/38.3/41.1/92.1
cable gland	99.4/37.9/43.2/98.2	98.9/26.4/34.8/96.3	95.2/14.4/23.1/86.8	97.8/ 46.0/49.8/64.1	98.4/25.2/32.0/94.5	99.4/39.5/43.9/98.4
carrot	99.4/27.5/33.7/97.2	98.0/12.2/19.3/93.4	96.4/13.8/21.2/84.4	86.9/26.5/21.7/14.2	98.6/20.0/26.9/94.6	99.4/30.1/35.4/98.1
cookie	96.6/27.5/32.9/86.6	97.5/40.4/45.6/88.7	90.5/26.7/31.4/66.6	93.3/34.0/35.6/40.9	94.3/14.0/23.8/83.5	96.8/39.0/41.9/83.6
dowel	99.7/47.7/50.8/98.8	99.1/32.1/37.7/96.1	95.3/17.4/25.6/83.0	97.3/43.1/44.5/31.2	97.2/31.4/40.1/89.6	99.6/49.9/50.4/97.1
foam	94.2/15.0/26.4/79.9	82.2/6.8/18.9/55.8	87.8/15.7/26.7/66.7	95.7/43.7/49.3/63.6	89.8/9.6/23.5/69.1	95.1/23.4/32.8/82.7
peach	98.5/15.5/22.7/93.2	97.4/11.7/17.9/90.4	92.9/8.1/15.0/74.8	95.9/35.7/41.2/48.2	98.4/27.6/31.3/94.2	99.4/43.2/45.1/97.1
potato	99.1/14.9/22.5/95.9	97.6/5.1/8.9/91.1	91.0/4.3/10.9/72.8	89.2/8.7/12.2/6.2	98.0/8.6/17.8/93.9	99.0/17.6/22.6/94.8
rope	99.6/50.3/55.9/97.9	99.0/34.5/40.7/94.3	99.3/51.1/52.9/92.8	98.8/64.5/62.1/90.4	99.3/61.0/59.9/96.5	99.4/52.1/50.9/95.5
tire	99.2/3.2/31.1/96.4	98.0/11.9/20.3/90.6	93.8/8.1/15.3/77.9	97.0/25.8/30.0/27.3	91.8/5.9/13.7/68.8	99.5/42.0/46.9/97.0
Mean	98.4/29.8/36.4/93.5	96.5/21.2/28.0/88.1	93.5/18.3/25.3/77.6	95.1/38.1/39.9/46.4	96.4/25.3/32.3/87.8	98.6/37.5/41.1/93.6

Table A7: Comparison with SOTA methods on **Uni-Medical** dataset for multi-class anomaly localization with AU-ROC/AP/F1_max metrics.

Method →	RD4AD [8] CVPR'22	UniAD [43] NeurIPS'22	SimpleNet [25] CVPR'23	DeSTSeg [49] CVPR'23	DiAD [14] AAAI'24	MambaAD (ours)
Category ↓						
brain	82.4/94.4/91.5	89.9/97.5/92.6	82.3/95.6/90.9	84.5/95.0/92.1	82.3/95.6/90.9	94.2/98.6/94.5
liver	55.1/46.3/64.1	55.1/46.3/64.1	55.8/47.6/60.9	69.2/60.6/64.7	55.8/47.6/60.9	63.2/53.1/64.7
retinal	89.2/86.7/78.5	84.6/79.4/73.9	88.8/87.6/78.6	88.3/83.8/79.2	88.8/87.6/78.6	93.6/88.7/86.6
Mean	75.6/75.8/78.0	78.5/75.2/76.6	75.6/76.9/76.8	80.7/79.8/78.7	75.6/76.9/76.8	83.7/80.1/82.0

Table A8: Comparison with SOTA methods on **Uni-Medical** dataset for multi-class anomaly localization with AU-ROC/AP/F1_max/AU-PRO metrics.

Method →	RD4AD [8] CVPR'22	UniAD [43] NeurIPS'22	SimpleNet [25] CVPR'23	DeSTSeg [49] CVPR'23	DiAD [14] AAAI'24	MambaAD (ours)
Category ↓						
brain	96.5/45.9/49.2/82.6	97.4/55.7/55.7/82.4	94.8/42.1/42.4/73.0	89.3/33.0/37.0/23.3	94.8/42.1/42.4/73.0	98.1/62.7/62.2/87.6
liver	96.6/5.7/10.3/89.9	97.1/7.8/13.7/ 92.7	97.4/13.2/20.1/86.3	79.4/21.9/28.5/20.3	97.1/13.7/7.3/91.4	96.9/9.1/16.3/91.8
retinal	96.4/64.7/60.9/86.5	94.8/49.3/51.3/79.9	95.5/59.5/56.3/82.1	91.0/59.0/46.8/31.7	95.5/59.5/56.3/82.1	95.7/64.5/63.4/83.1
Mean	96.5/38.7/40.1/86.4	96.4/37.6/40.2/85.0	95.9/38.3/39.6/80.5	86.6/38.0/37.5/25.1	95.9/38.3/39.6/80.5	96.9/45.4/47.3/87.5

E More Quantitative Results for Each Category on The COCO-AD Dataset.

Tab. A9 and Tab. A10 respectively present the results of image-level anomaly detection and pixel-level anomaly localization quantitative outcomes across all categories within the COCO-AD dataset. The results further demonstrate the superiority of our method over various SoTA approaches.

Table A9: Comparison with SOTA methods on **COCO-AD** dataset for multi-class anomaly detection with AU-ROC/AP/F1_max metrics.

Method →	RD4AD [8] CVPR'22	UniAD [43] NeurIPS'22	SimpleNet [25] CVPR'23	DeSTSeg [49] CVPR'23	DiAD [14] AAAI'24	MambaAD (ours)
Category ↓						
0	65.7/81.9/85.1	66.1/84.0/85.1	57.8/77.4/84.7	59.7/79.1/85.0	57.5/77.5/ 85.3	75.3/89.8/85.2
1	54.9/46.8/61.1	56.1/47.8/61.1	51.2/42.3/59.0	55.6/47.9/61.2	54.4/ 49.8/62.2	55.0/48.1/61.0
2	59.6/39.4/51.3	52.3/30.8/49.5	60.1/38.5/50.7	55.8/37.6/50.1	63.8/43.4/52.5	66.9/46.4/54.6
3	53.5/36.4/51.5	50.1/33.5/51.2	59.2/39.2/52.2	53.5/36.5/51.2	60.1/41.4/52.9	58.4/40.5/51.9
Mean	58.4/51.1/62.3	56.2/49.0/61.7	57.1/49.4/61.7	56.2/50.3/61.9	58.9/53.0/ 63.2	63.9/56.2/63.2

Table A10: Comparison with SOTA methods on **COCO-AD** dataset for multi-class anomaly localization with AU-ROC/AP/F1_max/AU-PRO metrics.

Method →	RD4AD [8] CVPR'22	UniAD [43] NeurIPS'22	SimpleNet [25] CVPR'23	DeSTSeg [49] CVPR'23	DiAD [14] AAAI'24	MambaAD (ours)
Category ↓						
0	72.1/30.8/38.2/45.9	70.8/29.4/36.7/36.5	64.0/27.4/34.4/26.8	61.8/21.5/27.7/23.5	67.0/33.4/26.2/28.8	75.6/38.6/41.7/46.2
1	70.7/6.2/11.2/40.6	70.0/6.2/11.3/31.8	61.4/4.9/8.9/33.0	69.3/6.8/11.3/27.7	71.3/11.8/7.8/28.8	71.2/6.6/11.3/36.6
2	68.4/11.6/18.9/42.9	60.9/7.7/14.7/27.0	57.4/8.2/14.4/29.2	61.1/9.8/13.9/26.3	68.0/19.2/12.2/33.2	71.2/13.9/21.6/44.4
3	58.3/8.4/14.2/33.4	59.8/8.3/ 14.8/31.4	55.3/8.2/13.9/21.0	51.2/6.9/12.4/16.8	65.9/17.5/10.6/32.3	59.0/8.6/14.4/ 34.7
Mean	67.4/14.3/20.6/ 40.7	65.4/12.9/19.4/31.7	59.5/12.2/17.9/27.5	60.9/11.3/16.3/23.6	68.0/20.5/14.2/30.8	69.3/16.9/22.2/40.5